BNL--46401

DE91 015840

EXAFS at Grazing Incidence: Data Collection and Analysis

S. M. Heald

Brookhaven National Laboratory, Upton NY 11973

Abstract

(Received)

EXAFS at grazing incidence can be applied to a large variety of surface and interface problems. This paper discusses in detail the collection and analysis of such data using interface EXAFS from metal/Al bilayers as an example. A comparison of the fluorescence and reflectivity detection channels is given, along with a discussion of the methods for correction of anomalous dispersion distortions. In addition, data from a Ni-Ti multilayer is used to demonstrate the potential of enhancing the sensitivity of the EXAFS signal to selected regions using standing wave effects.

PACS Nos. 78.70.D, 07.85

I. Introduction

The application of grazing incidence x-ray methods to surfaces and interfaces has grown rapidly in recent years. One technique which grazing incidence methods have impacted strongly is x-ray absorption fine structure (XAFS). The combination of grazing incidence with x-ray absorption allows detailed structural and chemical information to be obtained as a function of depth. This paper summarizes the current status of grazing incidence XAFS technique with an emphasis on data collection and analysis.

In 1954 Parratt [1] pointed out the potential of grazing incidence methods for structural studies of surfaces and presented a recursive method for calculating the properties of grazing incidence x-rays. The application to EXAFS began around 1980 [2-7] with most of the early efforts using detection of the reflected beam to determine the EXAFS. Greater sensitivity, however, can be obtained using fluorescence detection, with submonolayer sensitivity easily achieved.[5] More recently grazing incidence XAFS has been applied to a variety of surface and interface systems.[8-11] The application to buried interfaces is particularly interesting. Grazing incidence XAFS can provide structural information for buried interfaces out of reach of normal surface probes, and can study dilute or disordered systems which cannot be probed using grazing incidence diffraction methods.

II. Basics of grazing incidence X-rays

A. Anomalous Dispersion

For small enough incidence angles x-rays undergo total external reflection. This is a consequence of an index of refraction slightly less than one. The value of the index is proportional to the density of the material, with more dense materials having a larger critical angle, θ_c, below which total external reflection occurs. The index of refraction is normally written as $n = 1 - \delta - i\beta$. Near an absorption edge anomalous dispersion effects become important, and the real part of the absorption, δ, is modified. This is shown in Fig. 1 for Cu which shows the results of a Kramers-Kronig analysis for the energy dependence of δ near the Cu K absorption edge. The EXAFS oscillations in the absorption also appear in δ. At grazing incidence the reflectivity depends

on both the real and imaginary parts of n, and the structure in δ will affect the measured reflectivity or fluorescence from the sample. Thus, the measured spectra will be distorted, and must be corrected to obtain the true EXAFS signal. Since the δ oscillations are 90° out of phase with the normal EXAFS, the distortion results in a reduced amplitude as well as a phase shift.

Several methods have been presented for correcting the anomalous dispersion distortions.[6, 7, 12] These are based on a Kramers-Kronig type analysis or on approximations to calculate the energy dependence of δ. A Kramers-Kronig type analysis requires a knowledge of either δ or β over a long data range, but the experimental data is a combination of both. Poumellec *et al* [12] combine the two methods by assuming a $1/E^2$ dependence for the dispersion, and an arctan shape for the edge. The experimental data is then iteratively corrected and transformed until convergence is reached at the true absorption. This method works well for the signal from a surface, but would seem to have problems for multilayered systems. In our work a correction method has been demonstrated which relies on the fact that the EXAFS is a small perturbation on the atomic optical constants.[6, 13] Over the energy ranges typical in XAFS, the atomic optical constants can be well approximated by analytical expressions, and thus their energy dependence is easily calculated.[14, 15]

To carry out this approach for multilayer systems it is necessary to derive an accurate model of the reflectivity from the sample. This can be done by fitting the angular dependence of the reflectivity to obtain the depth dependent density profile.[16] Such a measurement of the reflectivity requires an extra step in the experiment, but is often useful in any case as a calibration of the sample angle, and as a guide for choosing the best angles for measuring the EXAFS. The density profile can then be obtained by fitting the reflectivity using the recursive calculation of Parratt[1] modified to include interface roughness.[17] Fig. 2 shows the results of such a fit for a Ni/Al bilayer sample. We have found that taking measurements both above and below the Ni edge improves the sensitivity of the fit.

Using the reflectivity model it is a simple matter to calculate the reflectivity or fluorescence in the absence of the EXAFS oscillations. For energies near the edge the analytic expressions are calibrated to the actual optical constants as available in tabulations.[18, 19] For either the reflectivity or fluorescence, the measured signal can be written as,

$$S = \mu G(\mu,\delta) \tag{1}$$

The absorption μ is composed of two parts: a smooth background, μ_0, and the small superimposed EXAFS oscillations, χ. Substituting $\mu = \mu_0 + \chi$ and expanding to first order in χ gives,

$$S = \mu_0 G_0 + \mu_0 \chi \frac{dG}{d\mu} + \chi G_0, \tag{2}$$

which can be written as,

$$\frac{S}{G_0} = \mu_0 + \chi[\,1 + \frac{\mu_0}{G_0}\frac{\partial G}{\partial \mu} + \frac{\mu_0}{G_0}\frac{\partial G}{\partial \delta}\frac{d\delta}{d\mu}]. \tag{3}$$

Again the quantity G_0 is calculated without the EXAFS oscillations. From this expression analyzing the function S/G_0 would give a χ' which is distorted by the expression in brackets. For fluorescence we analyze the function $S=I_f/I_0$, and for reflectivity the most convenient function is $S=\log(I_0/I_r)$ which is the same as for normal transmission. Using the log ratio eliminates the need to correct for the ion chamber response function. More details can be found in refs. 6 and 13 where they are applied to data from an Au surface. Excellent agreement with Au transmission data is found for both the corrected reflectivity and fluorescence signals. The fluorescence results are summarized in Table 1 which compares the EXAFS amplitudes before and after correction. It should also be noted that the correction factor in Eq. 3 is complex since the δ and β contributions are out of phase. Thus, there can also be small distortions of the EXAFS phases which can affect distance determinations. This is generally a small correction and is also found to be well treated by the above model.

B. Depth Sensitivity

After modeling the reflectivity it is a simple matter to calculate the penetration depth of the x-rays to determine the depth sensitivity. Fig. 3 shows a model calculation for the Cu/Al system.[20] In this case the sensitivity to a thin (50 Å) $CuAl_2$ interlayer is examined. For small angles the fluorescence is dominated by the Cu in the $CuAl_2$ layer even though the Cu density in this layer is only 0.28 that of the bulk Cu substrate. From the grazing incidence EXAFS interlayers of order of 10 Å are easily detected in these types of low-density on high-density systems.

Also shown in Fig. 3 is the penetration depth as a function of angle. For small angles it is relatively constant, but increases rapidly near the Cu critical angle. For an EXAFS scan it is necessary to vary the energy. Since the critical angle decreases as the energy increases, the

penetration into the sample can vary throughout the scan. For the case in Fig. 3 this effect is minor for angles well below the critical angle, but is important at larger angles. For a sample with a uniform composition over the region of maximum penetration this is not a problem, since the correction procedures described in the last section will remove the distortion to the EXAFS. However, for cases such as the example this can be a problem. As the penetration increases, the ratio of contributions from the Cu and $CuAl_2$ regions will change with the Cu region contributing more at the high energy end of the scan. This type of distortion can not be corrected since in an unknown sample the true EXAFS from a given region is not known. For these cases it is necessary to experimentally remove the changing penetration by varying the incidence angle as the energy is scanned.[6] In most cases a correction inversely proportional to the energy is satisfactory, although at the edge the anomalous dispersion change in δ can cause an additional change in the penetration.

III. Experimental

A. Apparatus

The basic experimental layout is shown in Fig. 4. The beam is collimated to a size such that it is smaller than the projected height of the sample at a fraction of the critical angle. For the samples discussed here which are 5 cm long, a beam size of 50-100 μm is adequate. At the NSLS this results in an incident flux of about 10^9 photons/sec on an unfocused beam line. Two different sample stages have been used. The more recent is based on a Huber 424 two circle goniometer with a ion chamber fluorescence detector. In this case exit slits slightly larger than the beam are used, and the reflectivity detector is a partially transmitting ion chamber followed by a NaI scintillation detector. This combination allows accurate reflectivity measurements over a dynamic range of about 10^7. Gear reduction and/or microstepping motors are used to achieve suitably small step size. When using angle correction during EXAFS data collection it is important that the motor steps are small enough that the sample is moved on each energy step, or high frequency artifacts may be introduced into the data.

Much of the early work used a simple flexure stage driven by a motorized micrometer. In this case no exit slit was used, and the angles were calibrated using photographs of the reflected

beam. When measuring the reflectivity near the critical angle the scattered background is negligible, and the exit slit is not needed to obtain accurate reflectivity measurements. An advantage of this stage is that its small weight and size means it can be easily mounted in almost any existing EXAFS station, including side stations with small clearance.

B. Sample preparation

Two types of samples will be discussed. The first is a Ni/Al bilayer structure. This was prepared in an ion-pumped all metal deposition chamber with a base pressure of 10^{-9} torr. The 1000 Å Ni layer is deposited onto a float glass substrate using a 30Å Cr binding layer, and covered with a 500 Å Al overlayer. All evaporations were done thermally using alumina or W boats, and the pressure during evaporation was typically 10^{-8} torr. It was found that the reactions at the interface are extremely sensitive to impurities,[21] and some additional samples were prepared with deliberate additions of O impurities. Only the clean sample will be discussed here.

Also discussed is data from a Ni-Ti multilayer. This was prepared by sputtering onto a float glass substrate using a system described elsewhere.[22] The layers are made by translating the substrate under two continuously running sputter guns. As the substrate is moved back and forth each layer is produced by two separate depositions. The multilayer was determined by x-rays to have a period of 120 Å with equal thickness layers.

IV. Experimental results and data correction

A. Ni-Al Bilayers

Figure 2 shows the reflectivity data for a clean Ni/Al bilayer taken at energies above and below the Ni absorption edge. When the Al critical angle is exceeded, the x-rays penetrate to the interface, and strong interference oscillations are observed. For fixed angle energy scans these lead to strong background modulations as shown for the fluorescence and reflectivity EXAFS signals in Fig. 5. To obtain the true EXAFS from these spectra requires two correction steps. First using the model which fits the reflectivity shown in Fig. 2, the function G_0 for the particular case is calculated and divided out. The resulting functions are also shown in Fig. 5, where it is seen that

most of the background has been removed. These spectra can now be analyzed in the usual fashion to obtain the EXAFS $\chi(k)$ interference function. This function is then corrected using Eq. 3 to obtain the true EXAFS from the interface. For this case the angles are small enough that the change in the penetration depth with energy is small enough to be ignored. This can be seen clearly in the fluorescence data. In spite of the large background modulation the overall slope of the fluorescence signal is fairly flat. For cases where the penetration is increasing the fluorescence signal would increase strongly at the high energy end of the scan.

The final corrected data are shown in Fig. 6, which compares the fluorescence and reflectivity results. Since these were taken at the same time they should be the same, but some differences can be seen in the amplitude. We believe part of the difference is a real experimental effect, and not a failure of the corrections. It comes from a contamination of the fluorescence signal caused by scattering of the incidence x-rays by the air, surface roughness, and the Al overlayer. A small fraction of x-rays are scattered to angles larger then the Ni critical angle, and penetrate into the substrate where they are absorbed causing additional fluorescence. Since the probed interface region is small, only a small amount of scattering is needed to cause a noticeable change in the measured fluorescence. To test this assumption EXAFS measurements were made at angles below the Al critical angle, where there should be no penetration to the Ni atoms in the interface or substrate. As expected the reflectivity showed essentially no absorption signal at the Ni absorption edge, while the fluorescence signal showed a small but distinct edge. Analysis of this signal showed it to be characteristic of pure Ni, verifying that it originated in the substrate, and was not due to Ni migration into the Al overlayer. As seen in Fig. 6 the magnitude of the effect for this case is less than the 10% accuracy typical of normal EXAFS, but for other experiments it could be larger and must always be considered when analyzing the fluorescence signal.

The EXAFS signal in Fig. 6 shows contributions for both Ni-Ni bonds and Ni-Al bonds. Detailed analysis indicated the formation of about 60 Å of a $NiAl_3$-like reacted region. Further analysis of this data along with O-exposed samples can be found in reference [21].

B. Ni-Ti Multilayer

The results for the Ni-Ti multilayer demonstrate the application of x-ray standing waves to enhance the sensitivity of grazing incidence EXAFS to selected regions in a multilayer structure. A brief discussion is given here. More details can be found in Ref. [22]. Fig. 7 shows a calculation for the reflectivity and the electric field intensity for a Ni-Ti multilayer. Near the first multilayer Bragg peak strong standing waves are set up with a period commensurate with the multilayer spacing. The phase of the standing wave can be varied by changing the angle slightly. The absorption is proportional to the standing wave intensity, and this allows the signal from different regions of the multilayer to be enhanced by adjusting the angle. For this experiment it is necessary to vary the incidence angle as the energy is scanned to maintain the same standing wave condition throughout.

The Ni-Ti system seemed to be an interesting case to study since Ni and Ti are known to undergo solid state amorphization reactions. For the sample studied, however, significant C and O contamination in the Ti layer has inhibited the reaction and little mixing of the Ni and Ti was observed. The existence of the standing wave could still be verified by studying the angular dependence of the Ni EXAFS as shown in Fig. 8. This data was taken in fluorescence, and since the samples are concentrated there is a significant reduction in the EXAFS amplitude due to a self-absorption effect.[23] The magnitude of the reduction depends on the effective Ni concentration. The standing wave effects change the relative absorption in the Ni layer as compared to the Ti layer, which is equivalent to changing the Ni concentration. As shown in Fig. 8 the observed angular dependence matches a calculation based on these ideas. This verifies that the standing waves are being excited with the expected amplitude.

V. Conclusions

Both the fluorescence and reflectivity signals can be corrected to obtain the actual EXAFS from a surface or interface region. As with bulk EXAFS the fluorescence signal is more sensitive, and can be applied to dilute samples or very thin regions. The sensitivity can easily be submonolayer. This sensitivity also makes the fluorescence channel less sensitive to spurious signals such as beam movement or monochromator "glitches". As discussed for the Ni-Al case scattering can cause a distortion of the fluorescence signal by increasing the contribution from the

substrate. If this is a concern then the reflectivity signal is a better choice. The reflectivity also has another advantage. For *in-situ* experiments only a small entrance and exit window are required, while fluorescence detection typically requires a large solid angle of detection to gain satisfactory signal.

A correction method has been presented with can be applied to both the fluorescence and reflectivity signals from complicated multilayer systems. The only requirement is that an accurate model of the x-ray reflectivity is obtained. This is generally straightforward for those cases for which the grazing incidence methods are applicable. Using this type of correction or those presented by others, the quantitative analysis of grazing incidence EXAFS should grow in application. The short range structural information available should provide a valuable complement to the information obtained from more standard methods.

V. Acknowledgements

This paper summarizes work which has spanned a number of years, and involved a number of collaborators. I would like to especially acknowledge the help of J. Tranquada and Hauiyu Chen in the initial studies on Au and Ni-Ti. They both also contributed to the development of the correction programs. For their contribution on the study of Ni-Al bilayers, I also thank E.V. Barrera, and J. Jayanetti. This work is supported by the U. S. Department of Energy, Division of Material Sciences under contract no. DE-AC02-76CH00016. The X-11 beamline is also supported by the DOE Division of Material Sciences under contract no. DE-AS05-80-ER10742.

References

1. L. G. Parratt, Phys. Rev. **95**, 359 (1954).

2. R. Barchewitz, M. Cremonse-Visicata and G. Onori, J. Phys. C **11**, 4439 (1978).

3. L. Bosio, R. Cortes, A. Defrain and M. Froment, J. Electroanal. Chem. **180**, 265 (1984).

4. R. Fox and S. J. Gurman, J. Phys. C **13**, L249 (1980).

5. S. M. Heald, E. Keller and E. A. Stern, Phys. Lett. A **103**, 155 (1984).

6. S. M. Heald, H. Chen and J. M. Tranquada, Phys. Rev. B **38**, 1016 (1988).

7. G. Martens and P. Rabe, Phys. Status Solidi A **58**, 415 (1980).

8. H. Chen and S. M. Heald, Physica **158**, 658 (1989).

9. N. T. Barrett, P. N. Gibson, G. N. Greaves, P. Mackle, K. J. Roberts and M. Sacchi, J. Phys. D **22**, 542 (1989).

10. G. N. Greaves, S. Pizzini, K. J. Roberts, N. T. Barrett and S. Kalbitzer, in *X-ray Absorption Fine Structure*, edited by S. S. Hasnain (Ellis Horwood, Chicester, 1991), p. 232.

11. T. M. Hayes, W. Li, G. Liang, C. M. Lo, T. E. Furtak, E. A. Creek, P. Samanta and L. Wang, in *X-ray Absorption Fine Structure*, edited by S. S. Hasnain (Ellis Horwood, Chicester, 1991), p. 229.

12. B. Poumellec, R. Cortes, F. Lagnel and G. Tourillon, Physica B **158**, 282 (1989).

13. H. Chen and S. M. Heald, Physica **158**, 322 (1989).

14. R. W. James, The Optical Principles of the Diffraction of X-rays (1958).

15. L. G. Parratt and C. F. Hempstead, Phys. Rev. **94**, 1593 (1954).

16. H. Chen and S. M. Heald, J. Appl. Phys **66**, 1793 (1989).

17. B. Vidal and P. Vincent, Appl. Opt. **23**, 1794 (1984).

18. W. H. McMaster, N. Kerr Del Grande, J. H. Mallett and J. H. Hubbell, Compilation of X-ray Cross Sections (1965).

19. D. T. Cromer, J. Appl. Cryst. **16**, 437 (1983).

20. S. M. Heald, H. Chen and J. M. Tranquada, J. de Physique **48-C8**, 825 (1986).

21. S. M. Heald and E. V. Barrera, J. Mater. Res. **6**, 935 (1991).

22. S. M. Heald and J. M. Tranquada, J. Appl. Phys **65**, 290 (1989).

23. Z. Tan, J. I. Budnick and S. M. Heald, Rev. Sci. Instrum. **60**, 1021 (1989).

Table 1

Comparison of the uncorrected and corrected EXAFS amplitudes obtained from the glancing angle fluorescence channel for various angles. These were obtained using the ratio method to compare the signals with transmission data from an Au foil. The critical angle for Au in this energy range is about 6.6mrad.

Angle (mrad)	Uncorrected	Corrected
3.12	0.90(3)	0.93(3)
4.15	0.90(3)	0.95(2)
5.17	0.86(5)	0.93(4)
6.20	0.74(4)	0.96(2)
7.23	0.41(3)	0.93(2)

Figure Captions

1. Kramer-Kronig calculation of δ for Cu metal near the Cu K-edge.

2. Reflectivity data (crosses) above and below the Ni K-edge for a Ni/Al bilayer sample. The lines are fits to the data using identical structural parameters for the two energies.

3. Calculated penetration depth and relative strength of the $CuAl_2$ fluorescence signal for the model shown in the inset. The penetration is measured from the top of the $CuAl_2$ layer which is 50 Å thick.

4. Schematic diagram of the experimental setup. The I_0, I and fluorescence detectors are ion chambers. The I detector is followed by a NaI scintillation detector. Slit S_1 defines the beam width, while the optional slits S_2 and S_3 are generally set somewhat larger, and are used to suppress scatter.

5. Raw (crosses) and corrected (lines) fluorescence and $\log(I_0/R)$ data from a Ni/Al bilayer sample.

6. Final corrected $\chi(k)$ data extracted from the fluorescence (dashed) and reflectivity (solid) channels.

7. a) Calculated (solid) and measured reflectivity (crosses) data for a Ni/Ti multilayer near the first order reflection peak. The smaller amplitude calculation includes 17 Å rms roughness at the interfaces, and matches the data well. b) Calculated electric field intensity normalized to the incident intensity for angles near the first order peak in a). The solid line and points are for 8.23 and 9.0 mrad respectively and include 17 Å roughness. For comparison the dashed line is calculated for 8.23 mrad with no roughness, and shows that the roughness does not strongly affect the standing wave intensity.

8. a) Fourier transform of the Ni EXAFS from the Ni-Ti multilayer at 8.02 (solid line) and 9.41 mrad

(dashed line). For comparison the points are the same transform for data obtained on a pure Ni foil. The right hand scale is for the foil data. b) Measured (points) and calculated EXAFS amplitudes for Ni first neighbor shell as a function of incident angle. The solid line assumes the normal Ti metal density, while the dashed curve is for a reduced density of 90%. The reduced density is probably more realistic since the Ti EXAFS indicated a substantial amount of low Z impurities.

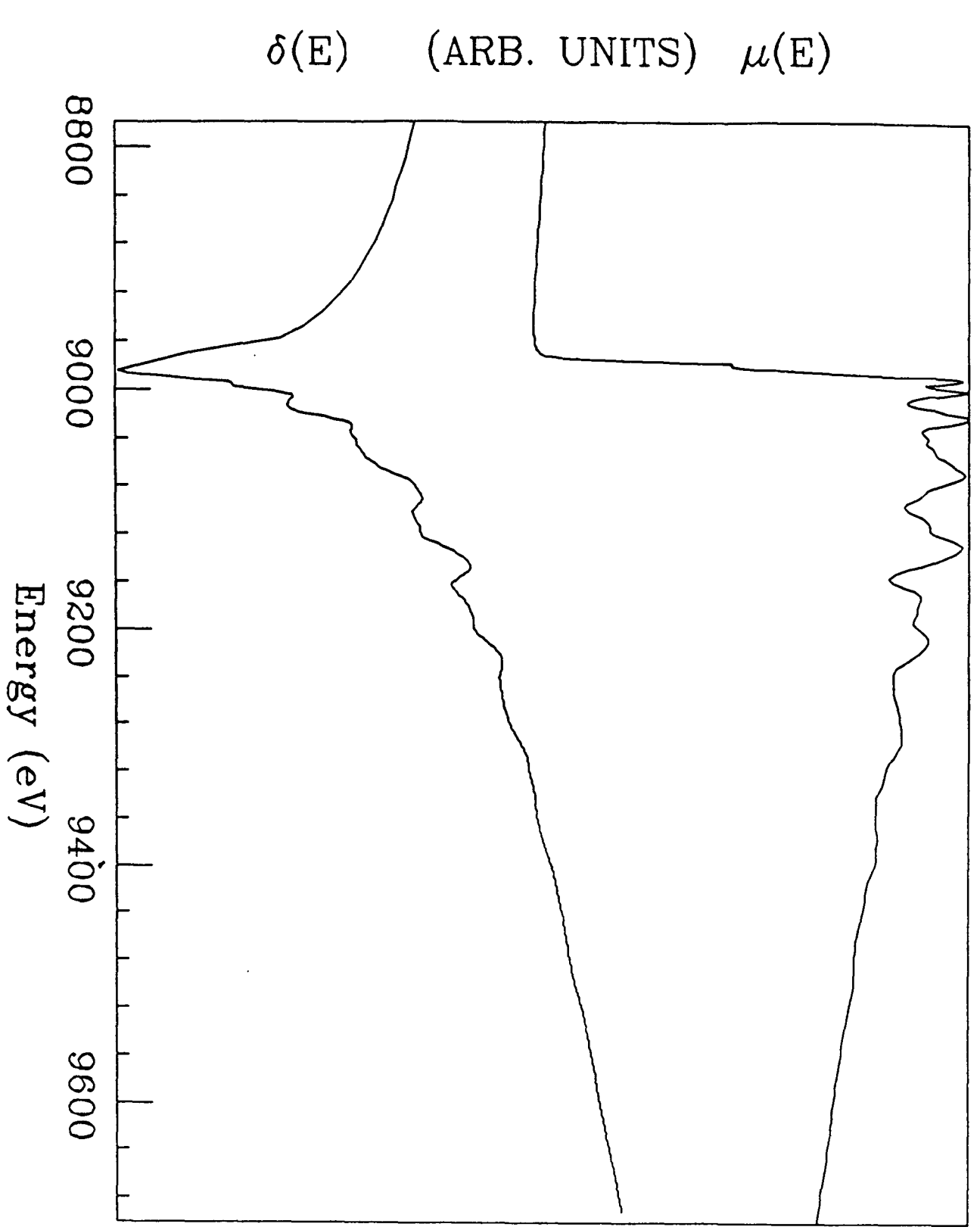

Fig. 1

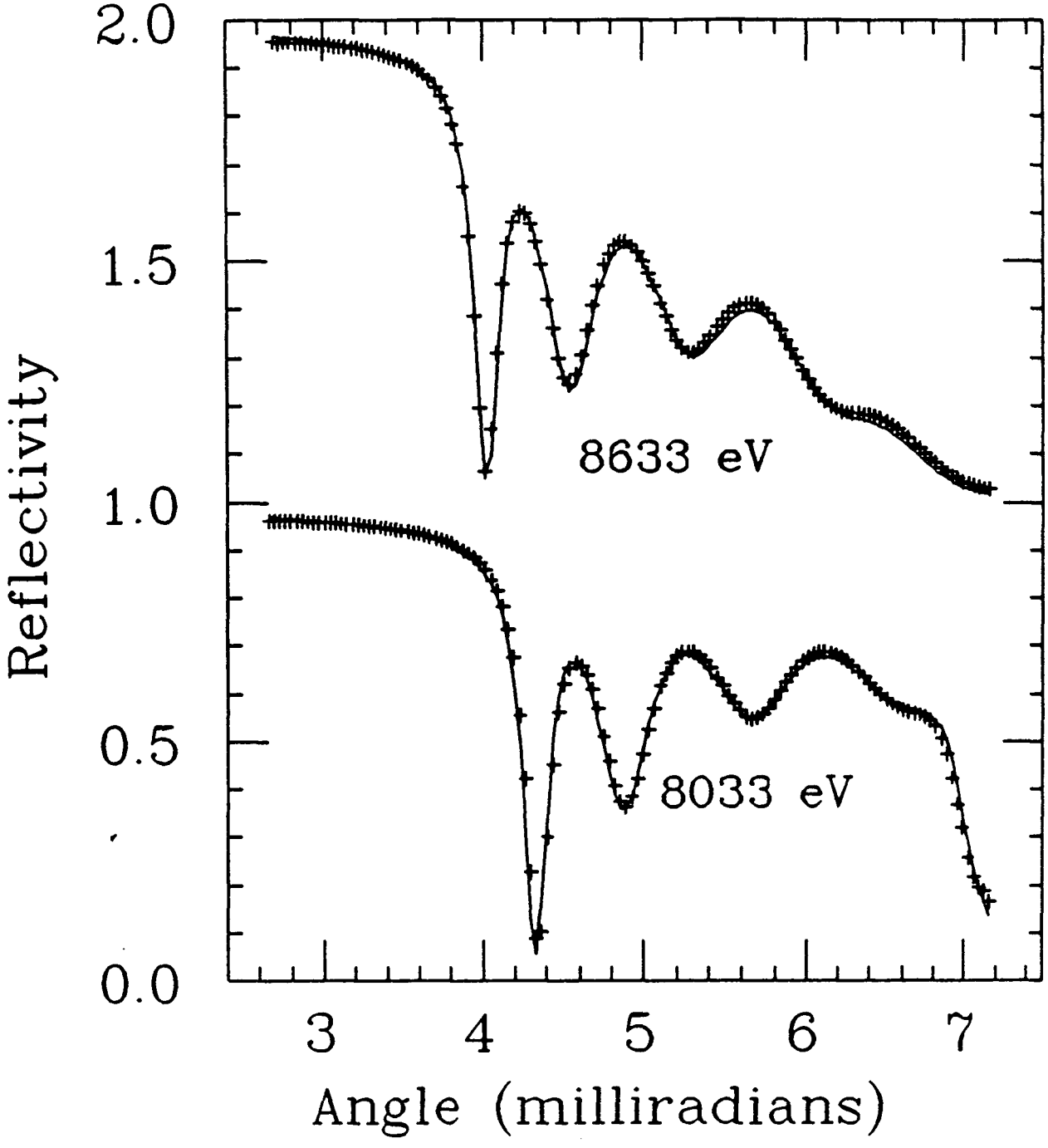
2.0
1.5
1.0
0.5
0.0
Reflectivity
8633 eV
8033 eV
3
4
5
6
7
Angle (milliradians)

Fig. 2

Fig. 5

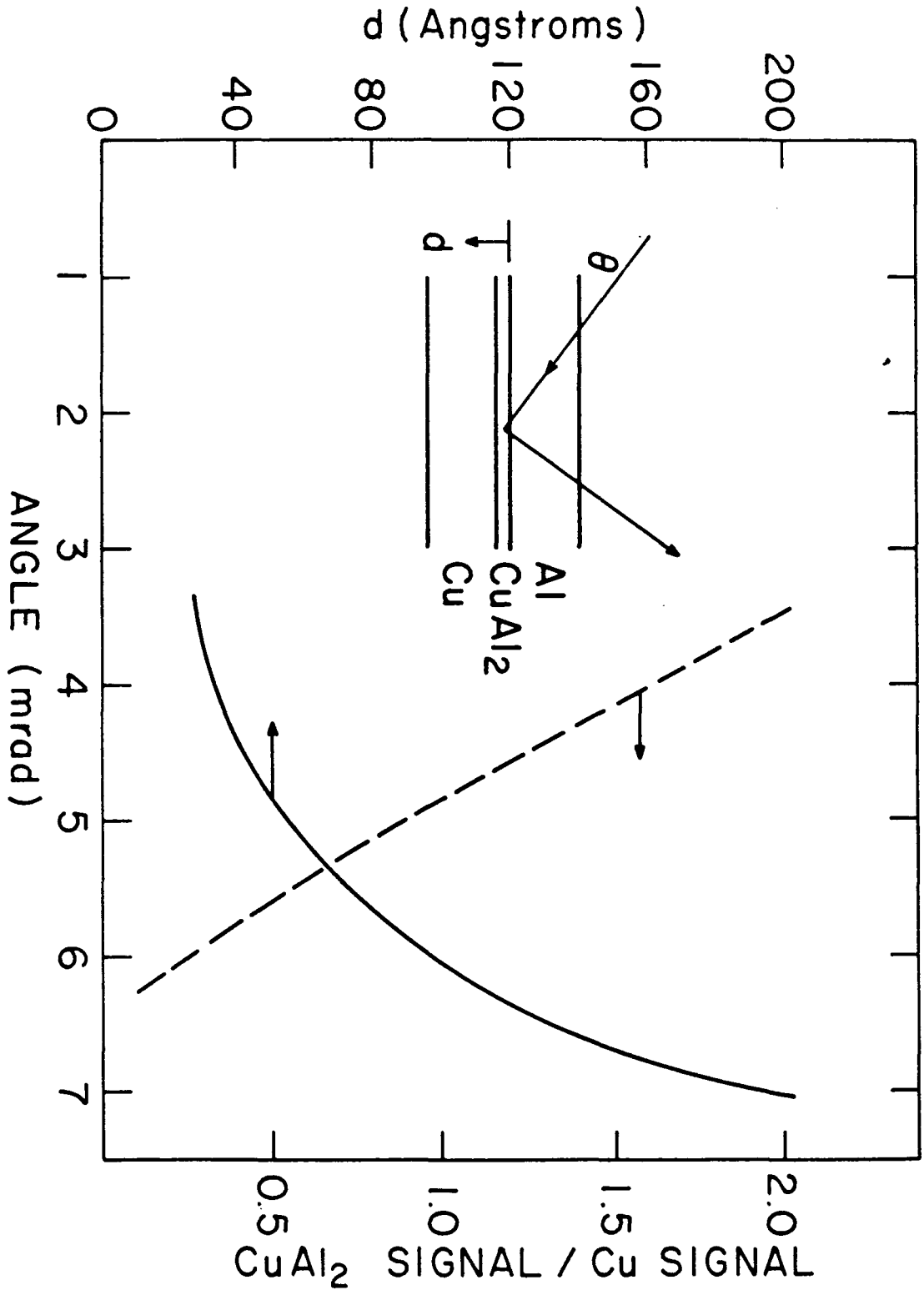
d (Angstroms)
0
40
80
120
160
200
ANGLE (mrad)
1
2
3
4
5
6
7
d
θ
Al
CuAl2
Cu
0.5
1.0
1.5
2.0
CuAl2 SIGNAL / Cu SIGNAL

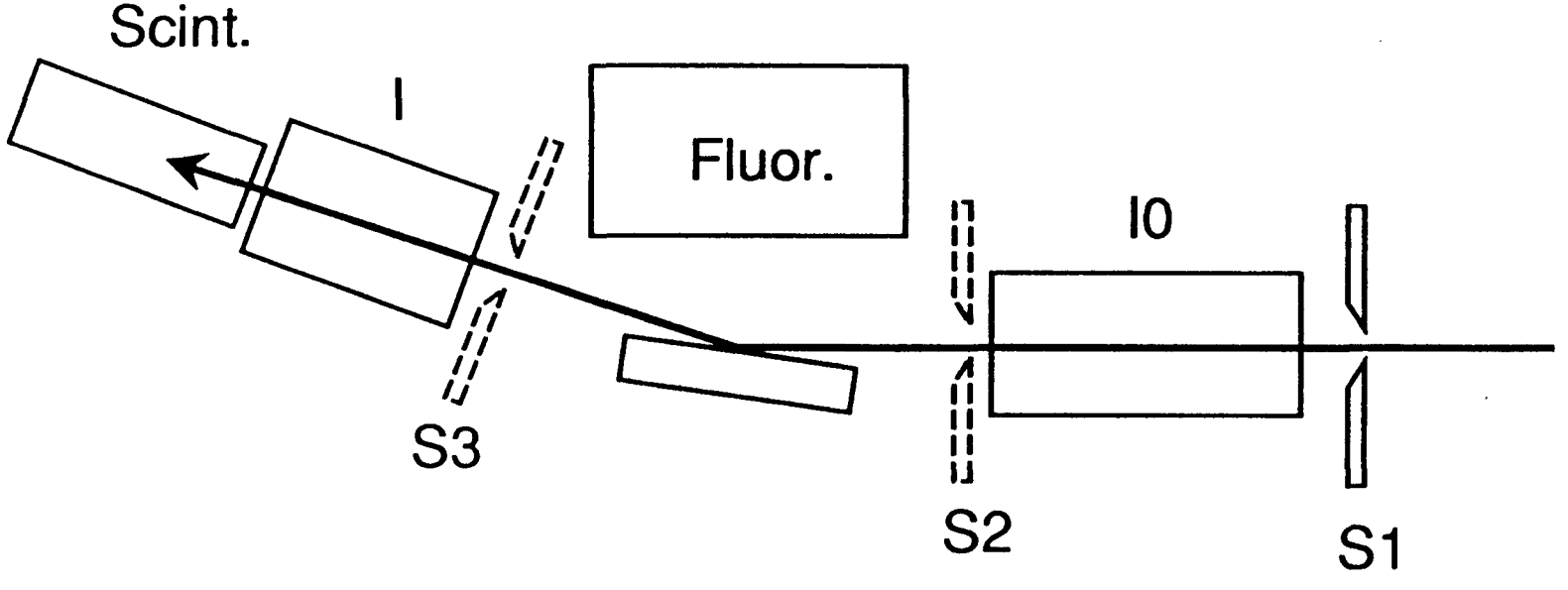

Fig. 4

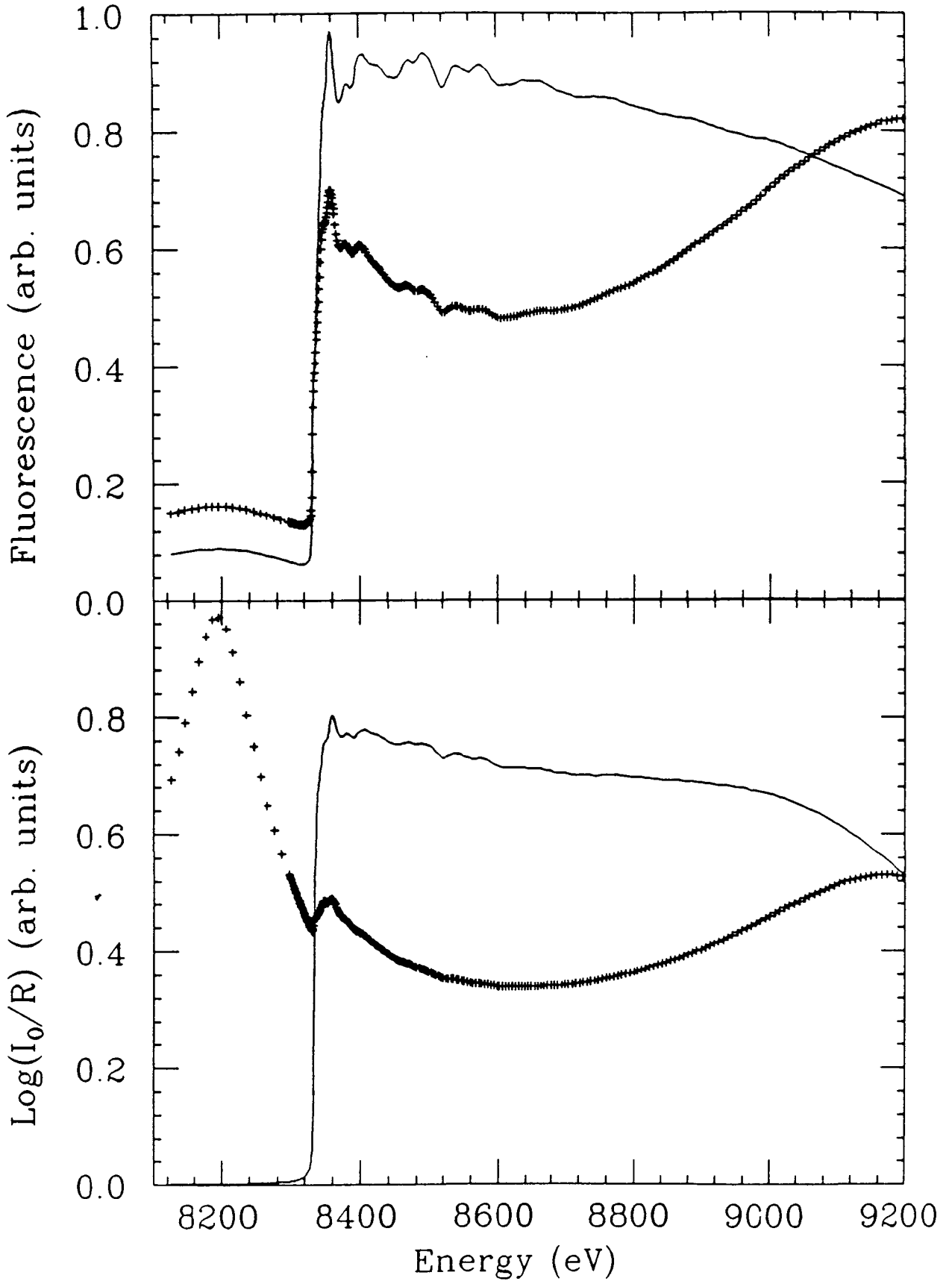
1.0
0.8
0.6
0.4
0.2
0.0
Fluorescence (arb. units)
0.8
0.6
0.4
0.2
0.0
Log(I0/R) (arb. units)
8200
8400
8600
8800
9000
9200
Energy (eV)

Fig. 5

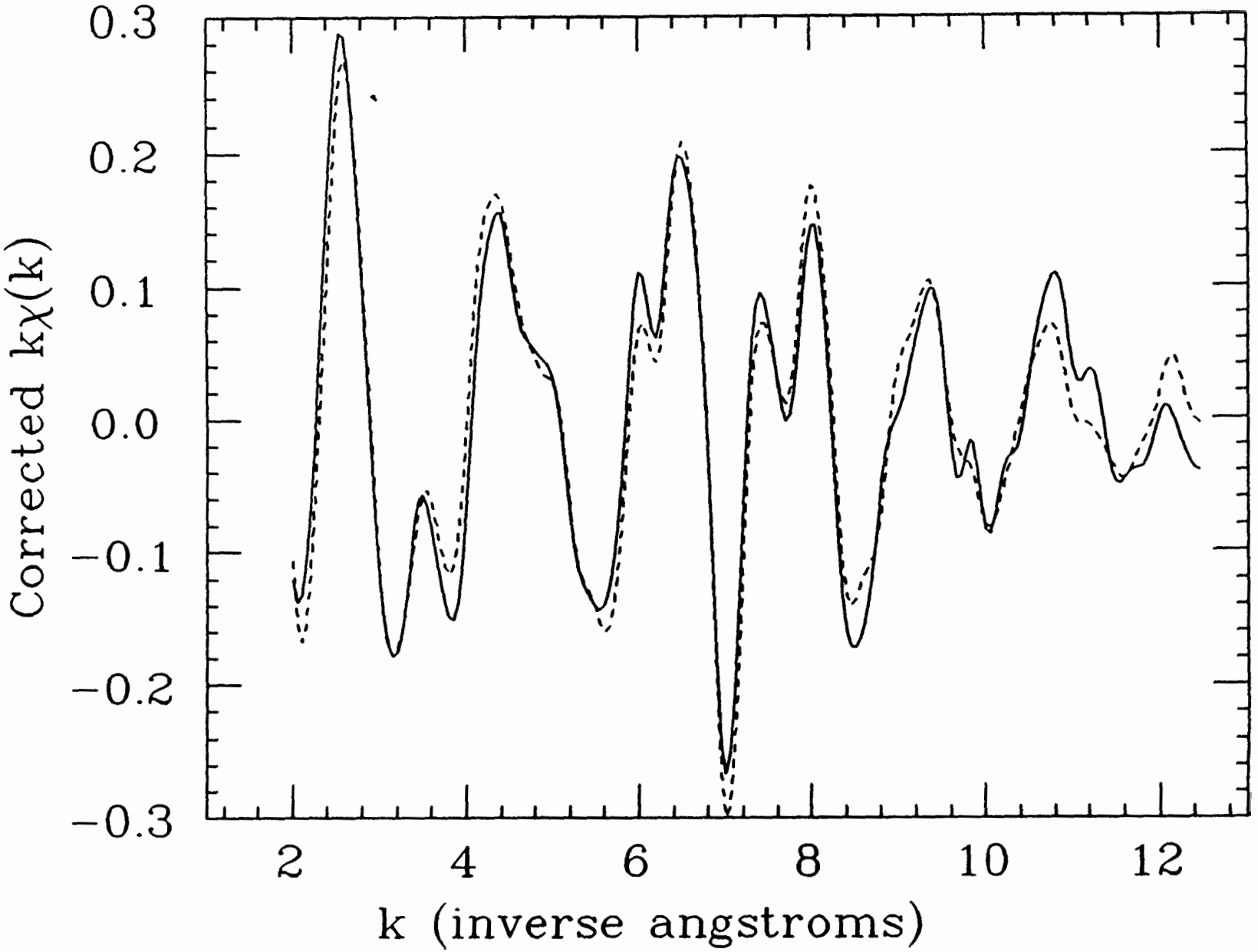
0.3
0.2
0.1
0.0
−0.1
−0.2
−0.3
Corrected kχ(k)
2
4
6
8
10
12
k (inverse angstroms)

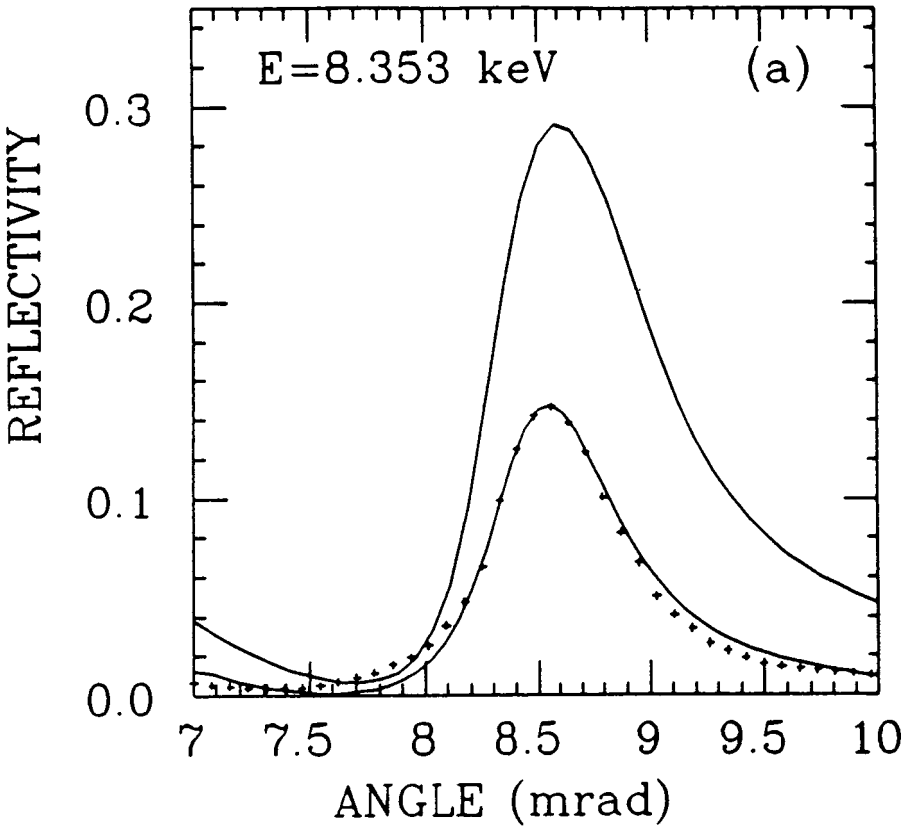
E=8.353 keV
(a)
REFLECTIVITY
0.3
0.2
0.1
0.0
7
7.5
8
8.5
9
9.5
10
ANGLE (mrad)

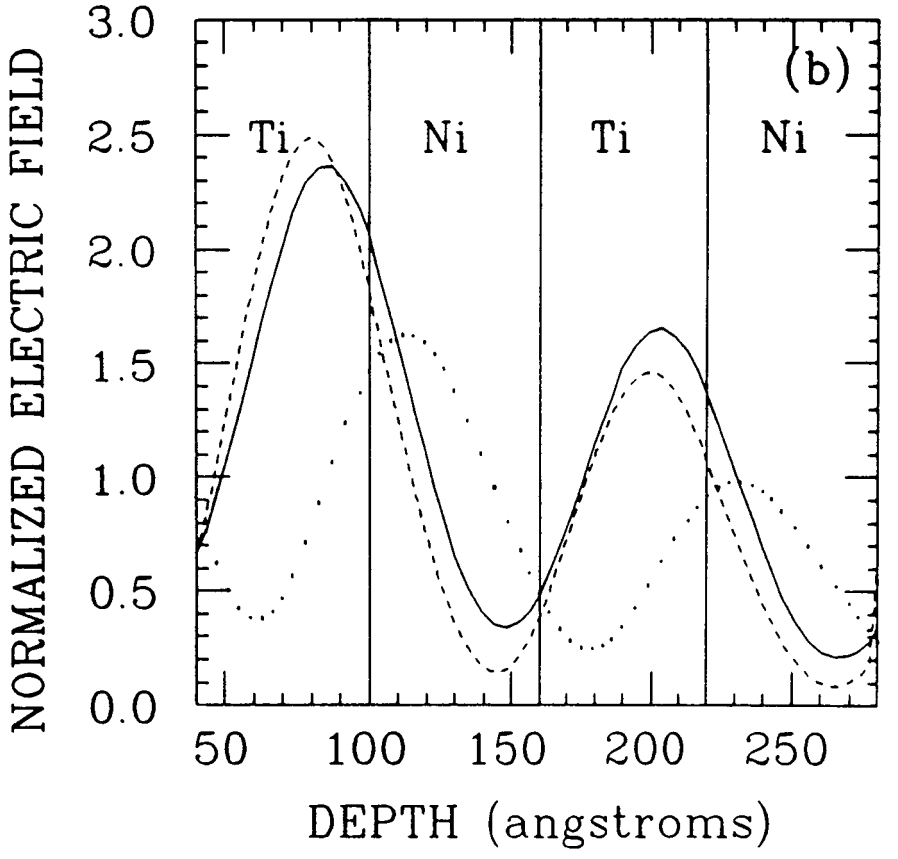
(b)
Ti
Ni
Ti
Ni
NORMALIZED ELECTRIC FIELD
3.0
2.5
2.0
1.5
1.0
0.5
0.0
50
100
150
200
250
DEPTH (angstroms)

Fig. 7

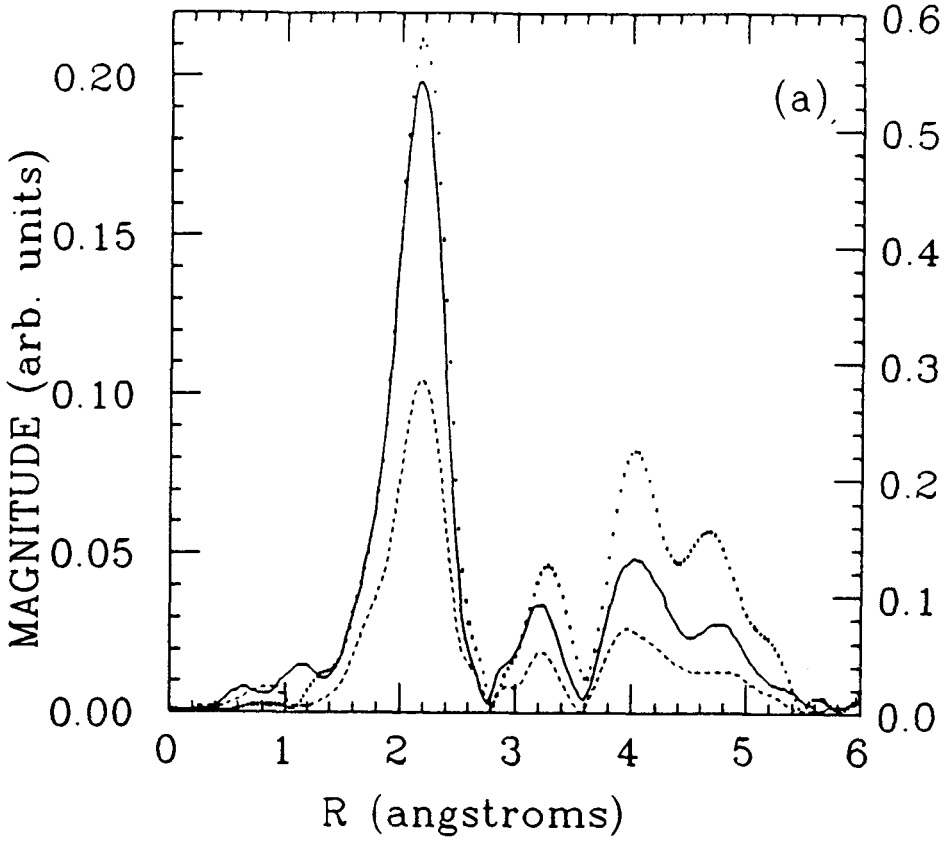
(a)
MAGNITUDE (arb. units)
0.00
0.05
0.10
0.15
0.20
0.0
0.1
0.2
0.3
0.4
0.5
0.6
0
1
2
3
4
5
6
R (angstroms)

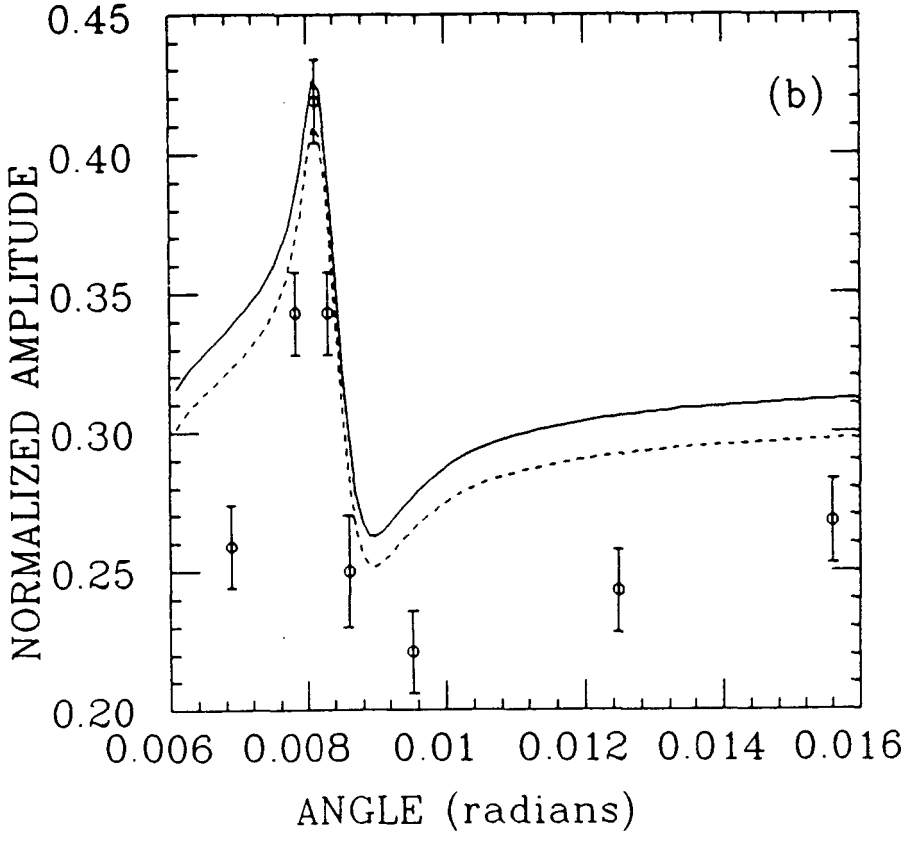
(b)
NORMALIZED AMPLITUDE
0.20
0.25
0.30
0.35
0.40
0.45
0.006
0.008
0.01
0.012
0.014
0.016
ANGLE (radians)

Fig. 8